Article

Not peer-reviewed version

Generalized Shear Correction Factor for Non-Homogeneous Beam Cross-Sections with an Embedded Steel Core

Anna Szymczak-Graczyk , Zijadin Guri , Ilir Canaj , Tomasz Garbowski *

Posted Date: 4 February 2026

doi: 10.20944/preprints202602.0160.v1

Keywords: Perlite composite; embedded steel core; hybrid beam; shear correction factor; Timoshenko theory; strain-energy equivalence; heterogeneous cross-section; voxel discretization

doi:10.20944/preprints202602.0160.v1

Article

Generalized Shear Correction Factor for Non-Homogeneous Beam Cross-Sections with an Embedded Steel Core

Anna Szymczak-Graczyk [1], Zijadin Guri [2] and Ilir Canaj [2] and Tomasz Garbowski [3,*]

[1] Department of Construction and Geoengineering, Poznan University of Life Sciences, Poznan, Poland
[2] Department of Structures, University of Prishtina, Prishtina, Kosovo
[3] University Center for Eco-materials, Poznan University of Life Sciences, Poznan, Poland
* Correspondence: tomasz.garbowski@up.poznan.pl

Abstract

Accurate prediction of transverse shear deformation is essential for the serviceability assessment, durability-oriented design, and structural health monitoring of hybrid and heterogeneous beam members. This is particularly relevant for lightweight composite components in which a porous cementitious matrix (e.g., perlite-based material) is combined with an embedded steel I-section, yielding strong stiffness contrasts and spatially nonuniform shear transfer. In this study, an energy-consistent analytical–numerical framework is proposed to determine the effective shear correction factor k_s for such non-homogeneous cross-sections within the Timoshenko beam theory. The formulation enforces equivalence between the real heterogeneous shear strain energy, governed by a spatial shear modulus field $G(y,z)$, and its beam-theory representation based on $k_s(G_{\mathrm{ref}}\,A)$. A pixel/voxel discretization is introduced to evaluate the generalized shear-energy integral and to quantify the deviation of k_s from classical homogeneous benchmarks. The results demonstrate that shear stiffness may be controlled by localized energy concentrations near weak matrix regions and phase interfaces, which can lead to non-negligible errors in deflection predictions when standard shear correction factors are adopted. The proposed framework provides a transparent and computationally efficient tool to support reliability-driven stiffness identification, model updating, and health monitoring strategies for heterogeneous and hybrid beam components.

Keywords: Perlite composite; embedded steel core; hybrid beam; shear correction factor; Timoshenko theory; strain-energy equivalence; heterogeneous cross-section; voxel discretization

---

1. Introduction

The growing demand for environmentally responsible construction solutions continues to reshape modern building technologies, stimulating the development and implementation of lightweight, low-carbon, and resource-efficient material systems [1–3]. Among these, expanded perlite has gained a particularly stable position as a readily available mineral aggregate enabling lightweight cementitious composites, thermal insulation components, and fire-related protection layers [4–6]. Recent studies underline that perlite-based mixtures can be engineered to provide a favorable balance between sustainability and performance, although their achievable mechanical response depends strongly on the binder system, the processing route, and the adopted composite architecture [7–9]. In parallel, perlite has been incorporated into polymer-based and hybrid porous composites to enhance mechanical functionality or thermostability in multi-phase systems, demonstrating the broader potential of porous architectures beyond conventional concrete technology [10–12].

While the use of perlite is frequently motivated by weight reduction and thermal efficiency, the structural adoption of porous eco-materials requires reliable prediction of deformation mechanisms,

 doi:10.20944/preprints202602.0160.v1

especially under combined bending and shear [13–16]. The key difficulty is that porous matrices are inherently heterogeneous: their microstructure contains nonuniform pore sizes, irregular void geometries, density gradients, and local necking-like effects, which collectively influence mechanical properties and stress redistribution [17–19]. Such variability directly affects the effective stiffness fields that govern global response and, in particular, the transverse shear mechanism that may dominate serviceability limits in short or moderately slender members [20,21]. For these reasons, porosity characterization and microstructure-informed modeling are increasingly recognized as indispensable components of modern durability-oriented structural assessment [17,22–24].

Transverse shear deformation is typically represented using reduced-order beam theories, most notably the Timoshenko formulation, which introduces an effective shear stiffness through a shear correction factor [25–27]. Although such representations are well established in classical solid mechanics and plate/beam theory, their standard correction factors assume homogeneous continua and do not account for stiffness fluctuations inside porous matrices or multi-phase cross-sections [28,29]. This is critical because even moderate errors in shear stiffness may propagate into inaccurate deflection predictions, biased stiffness identification, and unreliable assessment of structural condition under operational loads [30,31]. From the viewpoint of Structural Durability & Health Monitoring, this is not a cosmetic modeling detail: monitoring frameworks often interpret changes in global stiffness or displacement response as indicators of degradation, damage evolution, boundary-condition shifts, or long-term environmental impacts [32–34]. Therefore, shear-consistent reduced-order models are necessary to avoid misclassification of response changes in durability-related decision processes [35–38].

The modeling challenge becomes even more pronounced for hybrid beams, in which a porous matrix is combined with a stiff embedded reinforcement. One promising configuration is a beam composed of perlite-based matrix material strengthened by an embedded rolled steel I-section. Such members may offer an attractive compromise between sustainability (lightweight porous matrix) and robustness (steel load-carrying core), with potential relevance for prefabricated components and multi-functional elements [1,39–41]. At the same time, the steel insert introduces a strong stiffness contrast and a sharply non-homogeneous cross-section, leading to shear stress redistribution, energy localization near interfaces, and potential sensitivity to environmental actions such as moisture and temperature variations [42–44]. In this context, thermo-elastic effects and nonuniform stiffness fields may additionally influence effective shear correction factors, especially when material parameters depend on exposure conditions or functional gradients [29,45]. As a result, adopting classical homogeneous correction factors may become questionable for such hybrid cross-sections, particularly in serviceability-driven use cases.

Existing research has addressed parts of this problem, but the available approaches remain fragmented across different communities and scales. In civil engineering practice, effective material descriptions for perlite-based lightweight concretes are often derived from empirical or semi-empirical relationships and homogenized stiffness estimates [13–16,46]. In the broader mechanics community, mathematical homogenization frameworks and representative volume concepts have been developed to connect microstructural features to effective stiffness properties [47,48]. Complementarily, microstructure-resolved numerical models have been used to capture local stress concentrations and quantify effective responses for porous elastic systems with random inclusion distributions or reconstructed microgeometries [21,49] However, a direct translation of these high-resolution approaches to the shear correction factor required by Timoshenko-type beam models is not always straightforward, especially when the cross-section contains multiple phases with sharp stiffness discontinuities.

In recent years, data-driven strategies have also emerged, including machine-learning and deep-learning methods for parameter estimation, optimization, and predictive assessment in construction-related materials and geotechnical applications [33,50]. For durability and monitoring applications, digital twin concepts provide an additional layer of integration, enabling model updating and performance forecasting under changing environmental conditions [34,51]. Yet, even within digital

 doi:10.20944/preprints202602.0160.v1

twin workflows, reduced-order models remain the computational backbone for repeated evaluations, and their reliability hinges on consistent identification of effective stiffness parameters, including transverse shear stiffness. This highlights the need for a robust, transparent, and computationally efficient framework that links heterogeneous cross-sectional stiffness fields to an equivalent shear correction factor suitable for monitoring-oriented beam models.

To address these limitations, the present work proposes an energy-consistent analytical–numerical methodology for evaluating the shear correction factor k_s in non-homogeneous beam cross-sections consisting of a porous perlite-based matrix and an embedded steel I-core. The approach extends the classical strain-energy equivalence idea by explicitly incorporating a spatially varying shear modulus field and evaluating the heterogeneous shear-energy integral using a pixel/voxel discretization of the cross-section [52–54]. This makes it possible to quantify how stiffness contrast, porous heterogeneity, and phase distribution govern shear strain energy localization and the resulting effective transverse shear stiffness. The framework is compatible with multi-phase and microstructure-informed material descriptions and can be used as a practical component of stiffness identification and model updating procedures relevant to Structural Durability & Health Monitoring.

Finally, it is worth noting that perlite-based composites remain a particularly compelling case study due to their broad availability and established use in both cementitious and polymeric systems, as well as their role in fire-related performance contexts [54–59]. However, the same methodology is directly transferable to other porous eco-materials and hybrid structural members, including configurations with different porous aggregates or alternative reinforcement topologies [60–63]. By providing an explicit connection between heterogeneous shear strain energy and the macroscopic shear correction factor, the present work supports more reliable serviceability prediction and monitoring interpretation for lightweight hybrid beams.

2. Materials and Methods

A prismatic beam of length L, subjected to a transverse shear force V, is considered. The cross-section Aconsists of a non-homogeneous matrix material (perlite-based composite or cementitious matrix) with an embedded steel core in the form of a rolled I-section. The cross-sectional geometry is constant along the beam axis, while the material properties vary spatially within the section due to the stiffness contrast between the matrix and steel, and potentially due to matrix heterogeneity.

Within the framework of Timoshenko beam theory, the transverse shear strain is expressed as

$$\gamma_{xz}(y,z) = \theta(x) - \frac{\partial w(x)}{\partial x}, \tag{1}$$

where $w(x)$ denotes the transverse displacement of the beam axis and $\theta(x)$ is the rotation of the cross-section. The effective transverse shear stiffness is written as

$$K_{xz} = k_s\, G_{\mathrm{ref}}\, A, \tag{2}$$

where k_s is the shear correction factor and G_{ref} is a reference shear modulus introduced to maintain a Timoshenko-type representation.

For the actual shear stress distribution $\tau_{xz}(y,z)$, the transverse shear strain energy stored in the cross-section is given by

$$U_{\mathrm{real}} = \frac{1}{2}\int_A \frac{\tau_{xz}^2(y,z)}{G(y,z)}\, \mathrm{d}A, \tag{3}$$

where $G(y,z)$ denotes the local shear modulus, varying spatially due to heterogeneity.

The shear stress distribution resulting from cross-sectional equilibrium is expressed as

$$\tau_{xz}(y,z) = V\,\phi(y,z), \tag{4}$$

where $\phi(y,z)$ is the normalized shear-stress shape function satisfying

 doi:10.20944/preprints202602.0160.v1

$$\int_A \phi(y,z)\,\mathrm{d}A = 1. \tag{5}$$

Substitution into Eq. (3) yields

$$U_{\mathrm{real}} = \frac{V^2}{2}\int_A \frac{\phi^2(y,z)}{G(y,z)}\,\mathrm{d}A. \tag{6}$$

In the Timoshenko formulation, the transverse shear energy is written as

$$U_T = \frac{V^2}{2\,k_s\,G_{\mathrm{ref}}\,A}. \tag{7}$$

The shear correction factor k_s is identified by enforcing energy equivalence

$$U_{\mathrm{real}} = U_T. \tag{8}$$

Using Eqs. (6)–(8), the shear correction factor for a non-homogeneous cross-section becomes

$$k_s = \frac{1}{A\,G_{\mathrm{ref}}\displaystyle\int_A \frac{\phi^2(y,z)}{G(y,z)}\,\mathrm{d}A}. \tag{9}$$

For a homogeneous material $G(y,z) = G_{\mathrm{ref}}$, Eq. (9) reduces to the classical expression.

The function $\phi(y,z)$ depends only on geometry and equilibrium constraints. In the classical form used for prismatic sections, it may be written as

$$\phi(z) = \frac{Q(z)}{I\,b(z)}, \tag{10}$$

where $Q(z)$ is the first moment of area above the level z, I is the second moment of area about the neutral axis, and $b(z)$ is the local width at height z. In the present study, Eq. (10) is interpreted as a geometry-driven representation and is evaluated numerically for complex hybrid sections (matrix + embedded I-core), where $b(z)$ and $Q(z)$ reflect the combined area distribution of all phases.

The spatial distribution of shear modulus is defined as

$$G(y,z) = \begin{cases} G_m(y,z), & (y,z) \in A_{\mathrm{matrix}}, \\ G_s, & (y,z) \in A_{\mathrm{steel}}, \end{cases} \tag{11}$$

where G_s is the steel shear modulus and $G_m(y,z)$ corresponds to the matrix material. For porous matrices such as perlite composites, the modulus may depend on local density:

$$G_m(y,z) = G_0\,f\left(\frac{\rho(y,z)}{\rho_0}\right), \tag{12}$$

with $f(\cdot)$ calibrated experimentally.

To evaluate Eq. (9), the cross-section is discretized into surface elements (pixels/voxels) of area ΔA_i. The integral is approximated by

$$\int_A \frac{\phi^2}{G}\,\mathrm{d}A \approx \sum_{i=1}^{N} \frac{\phi_i^2}{G_i}\Delta A_i. \tag{13}$$

Accordingly, the discrete estimate becomes

$$k_s = \frac{1}{A\,G_{\mathrm{ref}}\sum_{i=1}^{N}\phi_i^2/G_i\,\Delta A_i}. \tag{14}$$

The discretization naturally accommodates sharp stiffness jumps (steel vs matrix) and can include void regions by introducing a material indicator field $\chi_i \in \{0,1\}$, where $\chi_i = 0$ corresponds to pores/voids (excluded from A and from the summation).

The reference modulus is introduced to keep Eq. (2) consistent with a Timoshenko-type representation. In this work, G_{ref} is taken as the nominal shear modulus of the matrix material, $G_{\mathrm{ref}} = G_m^{\mathrm{nom}}$, so that the computed k_s directly reflects the deviation caused by heterogeneity and the steel core. Alternative definitions (e.g., area-averaged $\langle G \rangle$ or maximum phase modulus) can also be adopted, and their influence may be assessed within a sensitivity analysis.

For comparison, the classical shear correction factor for a homogeneous rectangular cross-section is adopted

$$k_s^{\mathrm{ref}} = \frac{5}{6}. \tag{15}$$

The relative deviation due to heterogeneity is expressed as

$$\Delta k_s = \frac{k_s - k_s^{\mathrm{ref}}}{k_s^{\mathrm{ref}}}. \tag{16}$$

3. Results

This section presents the numerical identification of the shear correction factor k_s for a hybrid beam cross-section composed of a porous matrix and an embedded rolled steel I-section. The investigated configuration is a rectangular beam of dimensions $b \times h = 0.20 \times 0.30$ m with a centrally embedded IPE 200 core (Figure 1).

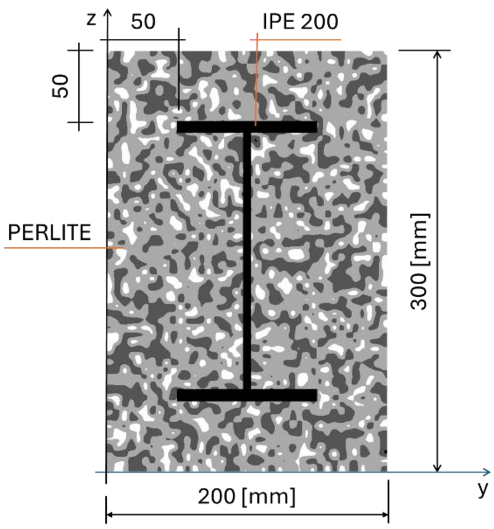

Figure 1. Cross-section of the hybrid beam composed of a porous matrix (perlite-based composite) and an embedded rolled steel I-section (IPE 200): geometry, coordinate system, and phase domains A_{matrix} and A_{steel}.

The evaluation follows the energy-equivalence formulation (Figure 2), combining the geometry-driven shear-stress function $\phi(y,z)$ with the heterogeneous shear modulus field $G(y,z)$ and voxel-based numerical integration (Table 1).

Voxelized 2D microstructure image,
Pixel size $\Delta y, \Delta z$,
Density–modulus relation $G(\rho)$,
Reference modulus $G_{\mathrm{ref}} = \int_A G(y,z) \,/\, A$.

 doi:10.20944/preprints202602.0160.v1

↓

Compute A, $\bar{z}$, I, b_j, Q_j.

↓

Compute φ_j.

↓

Compute k_s.

↓

Compute Δk_s.

Figure 2. Computational workflow of the proposed energy-consistent identification of the shear correction factor k_s for heterogeneous cross-sections: modulus field definition, evaluation of $\phi(y,z)$, voxel-based energy integral, and calculation of k_s and Δk_s.

The main outputs include the identified k_s, its deviation from the classical benchmark $k_s^{\mathrm{ref}} = 5/6$, the localization of heterogeneous shear energy ϕ^2/G, and monitoring-oriented implications for deflection-based stiffness interpretation.

Table 1. Discretization settings and convergence study for the identified shear correction factor k_s.

Grid ID	Pixel size [mm]	Number of pixels N [-]	Identified k_s [-]	Change vs finer grid [%]
G1	1.0	60 000	0.1682	11.24
G2	0.5	120 000	0.1734	8.496
G3	0.2	300 000	0.1845	2.639
G4	0.1	600 000	0.1895	-

The analyzed hybrid cross-section is shown in Figure 1 and summarized in Table 2. The matrix occupies the full 0.20×0.30 m rectangular envelope, while the IPE 200 steel section is placed centrally, introducing a sharp stiffness contrast between steel and the porous matrix.

Table 2. Geometric configuration of the analyzed hybrid cross-section (matrix envelope and embedded IPE 200 steel core).

Configuration ID	Matrix envelope [m]	Steel insert	Insert location	Total area A [m²]	A_{steel} [m²]	A_{steel}/A [%]
C1	0.20 × 0.30	IPE 200	centered	0.1200	0.00285	2.375

The adopted material parameters and reference modulus G_{ref} are reported in Table 3. For numerical evaluation of the heterogeneous energy integral (Eq. 14), the cross-section is discretized into pixels of area ΔA_i (Table 1), ensuring stable k_s values across grid refinements.

Table 3. Material parameters and modeling assumptions for the porous matrix and steel core, including reference modulus G_{ref}.

Phase	Young's modulus E [GPa]	Poisson's ratio ν [-]	Shear modulus G [GPa]	Notes
Matrix (homogenous)	35	0.20	14.0	Uniform case G_m =const.

Preprints.org (www.preprints.org) | NOT PEER-REVIEWED | Posted: 4 February 2026 doi:10.20944/preprints202602.0160.v1

Phase	Young's modulus E [GPa]	Poisson's ratio ν [-]	Shear modulus G [GPa]	Notes
Matrix (heterogeneous)	1–5	0.20	$G_m(y,z)$	From Eq. (12), density-driven
Steel (IPE 200)	210	0.30	80.8	$G_s = E_s/[2(1+\nu_s)]$
Reference	–	–	–	$G_{\mathrm{ref}} = \int_A G(y,z)\,/\,A$

The spatial distribution of the shear modulus $G(y,z)$ is illustrated in Figure 3. Two matrix descriptions are considered: (i) a uniform matrix modulus G_m, and (ii) a density-dependent heterogeneous modulus $G_m(y,z)$ reflecting spatial variability typical of porous eco-materials. In both cases, the steel phase retains a constant modulus G_s, resulting in a highly non-homogeneous stiffness field.

(a) **(b)**

Figure 3. Spatial distribution of the shear modulus $G(y,z)$ in the hybrid cross-section: (a) uniform matrix modulus G_m; (b) heterogeneous matrix modulus $G_m(y,z)$ derived from a density-dependent relation.

The normalized shear-stress shape function $\phi(y,z)$, evaluated for the matrix-only and hybrid sections, is shown in Figure 4. Since the shape function is reconstructed from purely geometric quantities (i.e., $Q(z)$, $b(z)$, and I), its spatial pattern is identical for both sections when the cross-sectional outline is unchanged. Consequently, the embedded I-section does not alter the equilibrium-based shear-transfer *shape* $\phi(y,z)$; instead, the effect of stiffness heterogeneity enters exclusively through the energetic weighting ϕ^2/G (Eq. 14), which changes the local contribution to shear strain energy and therefore the extracted effective shear stiffness.

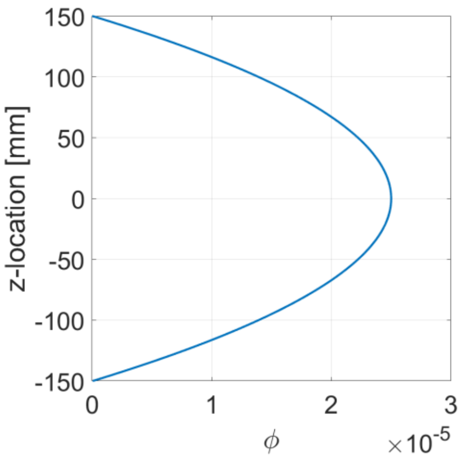

 doi:10.20944/preprints202602.0160.v1

Figure 4. Geometry-driven normalized shear-stress function $\phi(y,z)$ for both matrix-only cross-section and hybrid cross-section with embedded IPE 200 steel core.

This distinction is essential: while the shear-stress shape function $\phi(y,z)$ is entirely geometry-driven, the effective shear stiffness is obtained from its energetic projection, in which $\phi(y,z)$ is weighted by the local shear compliance $1/G(y,z)$. As a result, differences in material stiffness affect the contribution of individual regions to the total shear strain energy, without altering the equilibrium-based stress shape, and thus govern the identified value of k_s.

The heterogeneous shear-energy density indicator $\phi^2(y,z)/G(y,z)$ is presented in Figure 5. The maps reveal pronounced localization of shear strain energy within limited regions of the matrix phase, particularly in zones combining high shear demand with relatively low matrix stiffness. The embedded steel core reduces energy contributions inside the steel phase due to the high modulus G_s, but simultaneously enhances localization in surrounding matrix regions, especially near phase boundaries where ϕ remains significant.

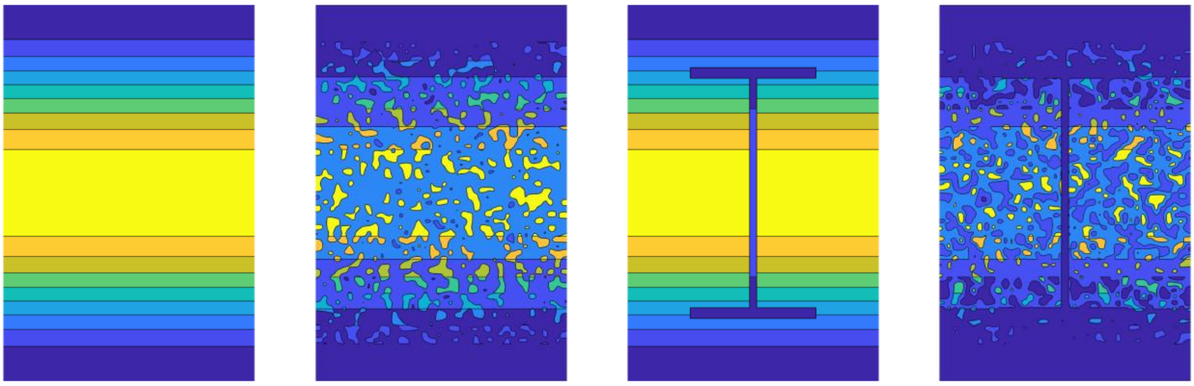

(**a**) (**b**) (**c**) (**d**)

Figure 5. Heterogeneous shear-energy density indicator $\phi^2(y,z)/G(y,z)$ in : (a) homogenous matrix-only cross-section; (b) heterogenous matrix-only cross-section; (c) hybrid homogenous cross-section with embedded IPE 200 steel core; (d) hybrid heterogenous cross-section with embedded IPE 200 steel core.

To quantify the role of each phase, the energy partition measures are summarized in Table 4. The results demonstrate that the global transverse shear response of the hybrid member may remain matrix-dominated, even though a stiff steel core is present. This observation supports the need for heterogeneous shear correction rather than relying on classical homogeneous factors, especially for monitoring-oriented stiffness interpretation.

Table 4. Partition of heterogeneous shear-energy contribution between steel and matrix phases based on the ϕ^2/G indicator.

Case	η_{steel} [%]	η_{matrix} [%]	Interpretation
H1 (homogenous)	6.5	93.5	matrix governs shear response
H2 (heterogeneous)	4.2	95.8	matrix dominance increases

To quantify the relative contribution of each material phase to the transverse shear response, the total shear-energy indicator is partitioned into phase-specific components. Based on the energetic formulation adopted in this study, the relevant quantity is the geometry-based shear-stress shape function $\phi(y,z)$, weighted by the local shear compliance $1/G(y,z)$.

The partial shear-energy indicators associated with the steel and matrix phases are defined as

 doi:10.20944/preprints202602.0160.v1

$$S_{\text{steel}} = \int_{A_{\text{steel}}} \frac{\phi^2(y,z)}{G_s(y,z)} \, \mathrm{d}A, \qquad S_{\text{matrix}} = \int_{A_{\text{matrix}}} \frac{\phi^2(y,z)}{G_m(y,z)} \, \mathrm{d}A. \tag{17}$$

These quantities represent the relative energetic weight of each phase under transverse shear, while the common multiplicative constants (such as the applied shear force or the factor $1/2$) cancel out when normalized measures are introduced. The total shear-energy indicator follows as the sum of the phase-specific contributions,

$$S_{\text{tot}} = S_{\text{steel}} + S_{\text{matrix}}. \tag{18}$$

The relative participation of each phase in the overall shear response is then expressed in terms of normalized energy fractions,

$$\eta_{\text{steel}}[\%] = 100 \, \frac{S_{\text{steel}}}{S_{\text{tot}}}, \qquad \eta_{\text{matrix}}[\%] = 100 \, \frac{S_{\text{matrix}}}{S_{\text{tot}}}. \tag{19}$$

By construction, these measures depend solely on the spatial overlap between the geometry-driven shape function $\phi(y,z)$and the local shear compliance distribution. Consequently, differences between homogeneous and heterogeneous configurations arise exclusively from the material-dependent weighting $1/G(y,z)$, while the equilibrium-based stress shape remains unchanged.

The identified k_s values obtained from Eq. (14) are summarized in Table 5 for the considered matrix descriptions. For the uniform matrix modulus case, the hybrid cross-section yields a k_s value that deviates from the classical benchmark $5/6$, indicating that the embedded steel core and stiffness contrast affect effective shear stiffness even when the matrix itself is assumed homogeneous. When matrix heterogeneity is introduced via $G_m(y,z)$, the deviation becomes more pronounced, reflecting additional energy localization in weaker matrix regions. The parametric trends are illustrated in Figure 6, where k_s is shown as a function of stiffness contrast and matrix stiffness level.

Table 5. Identified k_s and deviation from $5/6$

Case	Matrix model	k_s [-]	Δk_s [%]	G_{ref} [MPa]
M1	matrix-only (uniform)	0.833	-	14 000
M2	matrix-only (heterogonous)	0.664	-20.29	1 013
H1	hybrid + IPE 200 (homogeneous)	0.711	−14.65	17 019
H2	hybrid + IPE 200 (heterogeneous)	0.187	−77.55	4 967

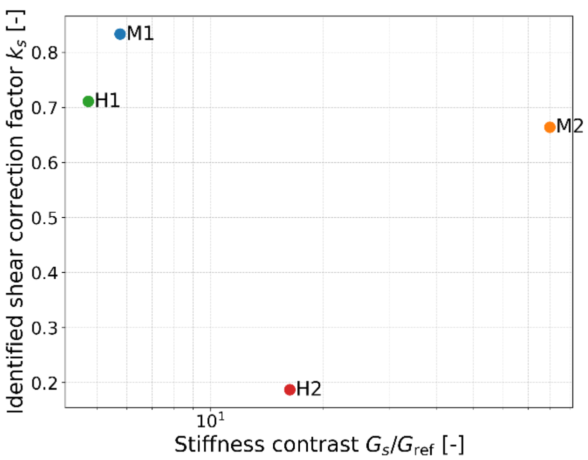

(a)

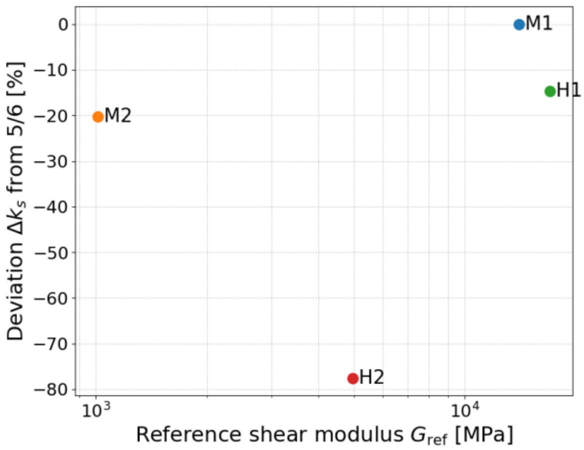

(b)

Figure 6. Parametric trends in the identified shear correction factor: (a) k_s as a function of stiffness contrast G_s/G_m; (b) deviation Δk_s versus matrix stiffness level and heterogeneity intensity.

In this sense, the classical value $k_s = 5/6$ should be regarded as a geometric reference rather than a robust approximation for hybrid porous members. The results confirm that the effective shear stiffness is controlled by heterogeneous energy redistribution rather than by geometry alone.

Figure 7 shows the mid-span deflection error arising from adopting the classical value $k_s = 5/6$ instead of the identified heterogeneous k_s. The error is reported for the considered matrix scenarios and illustrates that even moderate deviations in k_s may lead to systematic bias in displacement predictions.

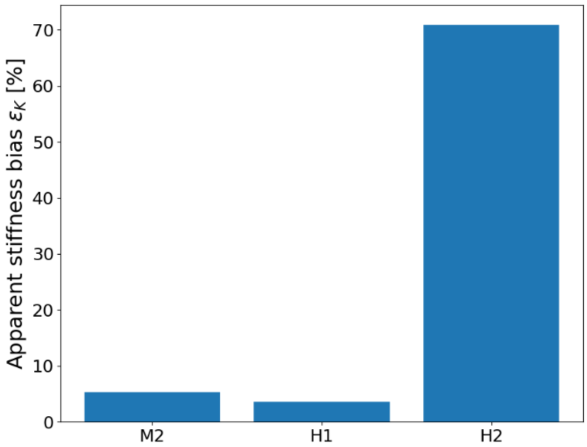

Figure 7. Serviceability and monitoring implication of using the classical shear correction factor: mid-span deflection error resulting from assuming $k_s = 5/6$ instead of the identified heterogeneous value.

To relate the identified shear correction factors to serviceability and monitoring-oriented interpretation, a simply supported beam of span L subjected to a concentrated transverse load P applied at mid-span is considered. The mid-span deflection is decomposed into a bending part (Euler–Bernoulli) and a shear part (Timoshenko), such that

$$w(k_s) = w_b + w_s(k_s). \tag{20}$$

The bending contribution at mid-span is governed by the Euler–Bernoulli expression

$$w_b = \frac{PL^3}{48\,EI_{\mathrm{ref}}}, \tag{21}$$

where E is the effective Young's modulus associated with bending and I is the second moment of area about the bending axis.

The shear contribution is expressed in terms of the effective shear stiffness $(GA)_{\mathrm{eff}} = k_s\,G_{\mathrm{ref}}\,A$ and reads

$$w_s(k_s) = \frac{PL}{4\,k_s\,G_{\mathrm{ref}}\,A}, \tag{22}$$

where A is the reference shear area of the cross-section and G_{ref} is the reference shear modulus used in the identification procedure.

To quantify the bias introduced by adopting the classical value $k_0 = 5/6$ instead of the identified value k_s, we define the relative mid-span deflection error as

$$\varepsilon_w[\%] = 100\,\frac{w(k_0) - w(k_s)}{w(k_s)}. \tag{23}$$

With this convention, $\varepsilon_w < 0$ indicates that using k_0 underestimates the deflection (i.e., the model appears artificially stiff in serviceability terms).

 doi:10.20944/preprints202602.0160.v1

Finally, to express the same effect in terms of monitoring-oriented stiffness interpretation, we introduce an apparent stiffness bias based on the inverse proportionality between stiffness and deflection, i.e. $K \propto 1/w$. The bias is therefore defined as

$$\varepsilon_K[\%] = 100\left(\frac{w(k_s)}{w(k_0)} - 1\right). \tag{24}$$

A positive ε_K corresponds to an overestimation of stiffness when the classical value k_0 is used in place of the identified heterogeneous value.

This has direct implications for monitoring workflows where measured deflections are interpreted through reduced-order models: if shear deformation is underestimated, the system may appear artificially compliant, which could be incorrectly attributed to bending stiffness degradation or damage accumulation. The monitoring-oriented metrics reported in Table 6 quantify these potential biases and highlight the importance of shear-consistent stiffness identification for hybrid perlite–steel members.

Table 6. Monitoring-oriented bias caused by adopting the classical shear correction factor $k_s = 5/6$ instead of the identified heterogeneous value, assuming L=1 m and P=1 kN.

Case	$(GA)_{\text{eff}}$ [MN]	$(EI)_{\text{eff}}$ [MNm²]	Mid-span deflection error ε_w [%]	Apparent stiffness bias ε_K [%]
M2	40.126	1.134	−5.08	+5.35
H1	726.42	18.81	−3.47	+3.59
H2	54.545	5.177	−41.5	+70.9

4. Discussion

The proposed formulation clearly separates two fundamentally different contributions to the transverse shear response. The normalized shear-stress shape function $\phi(y,z)$, introduced in Eqs. (4)–(5), is determined exclusively by the cross-sectional geometry through the classical equilibrium relations involving I, $Q(z)$, and $b(z)$. Consequently, for a fixed outer contour of the cross-section, $\phi(y,z)$ remains identical regardless of material heterogeneity or the presence of an embedded steel profile. This behavior is consistently observed in Figure 4, where the shape function exhibits the same spatial distribution for matrix-only and hybrid configurations sharing the same geometric outline.

In contrast, the effective shear stiffness and the associated shear correction factor k_s are governed by the energetic weighting introduced in Eq. (14), in which the geometry-driven function $\phi(y,z)$ is scaled by the local shear compliance $1/G(y,z)$. This distinction is essential for the interpretation of the results: material heterogeneity does not alter the equilibrium-based shear-stress shape but redistributes the contribution of individual regions to the total shear strain energy. The maps shown in Figure 5 directly reflect this mechanism, revealing strong variations in the indicator ϕ^2/G even when $\phi(y,z)$ itself remains unchanged.

The mesh convergence study summarized in Table 1 demonstrates that the identified values of $k_s$are numerically stable with respect to the pixel discretization used to evaluate the energy integral in Eq. (14). As the pixel resolution is refined, the changes in k_s diminish rapidly, indicating that the dominant energetic features of the shear response are sufficiently resolved. This observation is particularly relevant for heterogeneous cases, where localized regions of high ϕ^2/G may develop. The convergence results confirm that the proposed pixel-based integration scheme captures these localized effects without introducing mesh-dependent artifacts, thereby ensuring the reliability of the reported trends.

The role of the spatial distribution of the shear modulus $G(y,z)$ is highlighted by the comparison between uniform and heterogeneous matrix descriptions shown in Figure 3. When a constant matrix modulus is assumed, the energetic weighting remains relatively uniform across the

Preprints.org (www.preprints.org) | NOT PEER-REVIEWED | Posted: 4 February 2026 doi:10.20944/preprints202602.0160.v1

matrix domain. Introducing a spatially varying modulus, derived from the density-dependent relation in Eq. (12), leads to pronounced energetic localization, as evidenced by the distributions in Figure 5(b) and Figure 5(d).

These results illustrate that the effective shear response is controlled not merely by average material properties but by the spatial overlap between regions of high shear demand (large ϕ) and reduced local stiffness. The steel phase, characterized by a very high shear modulus (Table 3), contributes only marginally to the total shear energy, despite its structural presence. This effect is a direct consequence of the $1/G$ weighting and explains why the introduction of a stiff steel core does not necessarily lead to a steel-dominated shear response.

The phase-wise energy partition summarized in Table 4 provides a quantitative interpretation of the observations made in Figure 5. The low values of η_{steel} obtained for both hybrid cases indicate that the matrix phase governs the transverse shear response, even when a steel I-section is embedded within the cross-section. This finding underscores the energetic nature of the shear correction factor: regions with low shear compliance dominate the equilibrium stress field, whereas regions with higher compliance dominate the energy balance.

From a modeling perspective, this result emphasizes that the effective shear stiffness cannot be inferred from geometric considerations or stiffness contrasts alone. Instead, it emerges from the combined effect of geometry-driven stress distribution and material-dependent energetic weighting, as formalized in Eqs. (17)–(19).

The identified values of k_s summarized in Table 5 reveal substantial deviations from the classical reference value $k_s = 5/6$, particularly for heterogeneous configurations. Figure 6(a) shows that k_s decreases systematically with increasing stiffness contrast between steel and matrix phases, while Figure 6(b) highlights the dependence of Δk_s on the reference shear modulus and the degree of heterogeneity.

These trends confirm that the classical shear correction factor should be regarded as a geometric benchmark applicable primarily to homogeneous sections. For hybrid or porous members with spatially varying material properties, the effective shear correction factor is inherently problem-specific and must be identified through an energetically consistent procedure.

The practical consequences of adopting an inappropriate shear correction factor are demonstrated in Figure 7 and Table 6, where the mid-span deflection error and the apparent stiffness bias are evaluated for a simply supported beam subjected to a central point load. The results show that even moderate deviations in k_s can lead to non-negligible errors in deflection predictions. In monitoring-oriented applications, such discrepancies may be misinterpreted as changes in structural stiffness or damage progression.

The presented results therefore highlight the importance of using a shear correction factor that is consistent with the actual material heterogeneity of the member. In the context of eco-materials and hybrid structures, where material properties may evolve over time due to environmental exposure or degradation, the proposed methodology offers a physically grounded framework for updating shear-related parameters in reduced-order models.

5. Conclusions

This study presented an energetically consistent framework for identifying the transverse shear correction factor k_s in heterogeneous and hybrid beam cross-sections. By explicitly separating the geometry-driven shear-stress shape function from the material-dependent energy weighting, the proposed method provides a clear physical interpretation of how spatial variations in shear modulus influence the effective shear stiffness.

The results demonstrate that, for a fixed cross-sectional outline, the shear-stress shape function remains purely geometric, while deviations in k_s arise solely from heterogeneous energy redistribution. In hybrid sections with an embedded steel core, the shear response may remain dominated by the matrix phase, despite the high stiffness of the steel component. This behavior cannot be captured by classical homogeneous shear correction factors.

Parametric studies and deflection-based assessments further showed that adopting the classical value $k_s = 5/6$ may introduce systematic errors in serviceability predictions and monitoring-based stiffness identification. The proposed pixel-based energy integration approach therefore constitutes a practical and robust tool for evaluating shear correction factors in modern hybrid and eco-material structures, where material heterogeneity plays a decisive role in the transverse shear response.

Author Contributions: The authors confirm contribution to the paper as follows: Conceptualization, T.G. and A.S.-G.; methodology, T.G. and A.S.-G.; software, T.G.; validation, Z.G., I.C.; formal analysis, A.S.-G., I.C. ; investigation, T.G. and Z.G.; resources, Z.G. and I.C; data curation, Z.G. and I.C.; writing—original draft preparation, T.G.; writing—review and editing, A.S.-.G.; visualization, A.S.-G. and T.G.; supervision, A.S.-G. and T.G.; project administration, A.S.-G. and T.G.; funding acquisition, T.G. All authors reviewed and approved the final version of the manuscript.

Funding Statement: The author(s) received no specific funding for this study.

Acknowledgments: None.

Conflicts of Interest: The authors declare no conflicts of interest.

Availability of Data and Materials: The data that support the findings of this study are available from the Corresponding Author upon reasonable request.

Ethics Approval: Not applicable.

References

1. Rashad, A.M. A synopsis about perlite as building material: A best practice guide for civil engineers. Constr. Build. Mater. 2016, 121, 338–353. https://doi.org/10.1016/j.conbuildmat.2016.06.001
2. Abed, A.T.; Éva, L. A comprehensive study of perlite in building materials: Balancing sustainability and performance. J. Therm. Anal. Calorim. 2025, 150, 10627–10643. https://doi.org/10.1007/s10973-025-14410-6
3. Dzięcioł, J.; Szlachetka, O. Waste or raw material? Perlite concrete as part of a sustainable materials management process in the construction sector. Sustainability 2024, 16, 6818. https://doi.org/10.3390/su16166818
4. Koukouzas, N.K.; Dunham, A.C.; Scott, P.W. Suitability of Greek perlite for industrial applications. Trans. Inst. Min. Metall. B 2000, 109, 105–111.
5. Jia, G.; Li, Z.; Liu, P.; Jing, Q. Preparation and characterization of aerogel/expanded perlite composite as building thermal insulation material. J. Non-Cryst. Solids 2018, 482, 192–202.
6. Ariyaratne, I.E.; Ariyanayagam, A.; Mahendran, M. Bushfire-resistant lightweight masonry blocks with expanded perlite aggregate. Fire 2022, 5, 132. https://doi.org/10.3390/fire5050132
7. Cojocaru, A.; Isopescu, D.N.; Maxineasa, S.G. Perlite concrete: A review. IOP Conf. Ser. Mater. Sci. Eng. 2023, 1283.
8. Topçu, I.B.; Işıkdağ, B. Effect of expanded perlite aggregate on the properties of lightweight concrete. J. Mater. Process. Technol. 2008, 198, 134–138.
9. Singh, M.; Garg, M. Perlite-based building materials: A review of current applications. Constr. Build. Mater. 1991, 5, 75–81.
10. Qiao, Y.; Bian, X.; Ke, H.; Zhao, Z.; Zhang, X.; Zhang, X.; Zhao, Y.; Bai, C.; Zhang, L.; Zheng, T.; et al. Phenolic-based porous composite with embedded short carbon fiber/hollow spheres for mechanical properties and thermostability. Compos. Commun. 2025, 55, 102305. https://doi.org/10.1016/j.coco.2025.102305
11. Ciminli, A.T.; Bulut, H.A. A new approach for lightweight polymer concrete production: Influence of resin and perlite types on mechanical performance. Constr. Build. Mater. 2025, 490, 142608. https://doi.org/10.1016/j.conbuildmat.2025.142608

 doi:10.20944/preprints202602.0160.v1

12. Mattausch, H.I.; Laske, S.; Cirar, K.; Flachberger, H.; Holzer, C. Fundamental investigations of reinforcement of expanded perlite in polypropylene. In New Developments in Polymer Composites Research; Nova Science Publishers: New York, NY, USA, 2013; pp. 213–226.
13. Erdem, T.K.; Meral, C.; Tokyay, M.; Erdoğan, T.Y. Use of perlite as a pozzolanic addition in producing blended cements. Cem. Concr. Compos. 2007, 29, 13–21.
14. Sengul, O.; Azizi, S.; Karaosmanoglu, F.; Tasdemir, M.A. Effect of expanded perlite on the mechanical properties and thermal conductivity of lightweight concrete. Energy Build. 2011, 43, 671–676.
15. Demirboğa, R.; Örüng, I.; Gül, R. Effects of expanded perlite aggregate and mineral admixtures on the compressive strength of low-density concretes. Cem. Concr. Res. 2001. https://doi.org/10.1016/S0008-8846(01)00615-9
16. Jedidi, M.; Benjeddou, O.; Soussi, C. Effect of expanded perlite aggregate dosage on properties of lightweight concrete. Jordan J. Civ. Eng. 2015, 9, 278–291. https://doi.org/10.14525/jjce.9.3.3071
17. da Silva, M.T.Q.S.; Perretto, F.; do Rocio Cardoso, M.; Mazer, W. Porosity: Some characterization techniques. Mater. Today Proc. 2023. https://doi.org/10.1016/j.matpr.2023.03.716
18. Taherishargh, M.; Belova, I.V.; Murch, G.E.; Fiedler, T. Effect of particle shape on mechanical properties of perlite/metal syntactic foam. J. Alloys Compd. 2017, 693. https://doi.org/10.1016/j.jallcom.2016.09.168
19. Burriesci, N.; Arcoraci, C.; Antonucci, P.L.; Polizzotti, G. Physico-chemical characterization of perlite of various origins. Mater. Lett. 1985, 3, 103–110.
20. Alexa-Stratulat, S.M.; Taranu, G.; Toma, A.M.; Olteanu, I.; Pastia, C.; Bunea, G.; et al. Effect of expanded perlite aggregates and temperature on strength and dynamic elastic properties of cement mortar. Constr. Build. Mater. 2024, 438, 137229. https://doi.org/10.1016/j.conbuildmat.2024.137229
21. Chen, K.; Qin, H.; Ren, Z. Establishment of the microstructure of porous materials and its relationship with effective mechanical properties. Sci. Rep. 2023, 13, 18064. https://doi.org/10.1038/s41598-023-43439-6
22. Khanna, P.; Mukulam, A.M.; Teja, K.V.; Meena, T. Study on durability properties of perlite incorporated concrete. Int. J. Civ. Eng. Technol. 2018, 9, 1545–1553.
23. Buljak, V.; Cocchetti, G.; Cornaggia, A.; Maier, G. Estimation of residual stresses by inverse analysis based on experimental data from sample removal for small punch tests. Eng. Struct. 2017, 136, 77–86. https://doi.org/10.1016/j.engstruct.2017.01.010
24. Cornaggia, A.; Gajewski, T.; Garbowski, T.; Knitter-Piątkowska, A. Simulating fiber-reinforced concrete mechanical performance using CT-based fiber orientation data. Materials 2019, 12, 717. https://doi.org/10.3390/ma12050717
25. Timoshenko, S.; Woinowsky-Krieger, S. Theory of Plates and Shells; Arkady: Warsaw, Poland, 1962.
26. Donnell, L.H. Beams, Plates and Shells; McGraw-Hill: New York, NY, USA, 1976.
27. Carrera, E.; Giunta, G.; Petrolo, M. Beam Structures: Classical and Advanced Theories; John Wiley & Sons: Chichester, UK, 2011. https://doi.org/10.1002/9781119978565
28. Kączkowski, Z. Płyty: Obliczenia Statyczne; Arkady: Warsaw, Poland, 2000.
29. Lim, T.-K.; Kim, J.-H. Thermo-elastic effects on shear correction factors for functionally graded beams. Compos. Part B Eng. 2017, 123, 262–270. https://doi.org/10.1016/j.compositesb.2017.05.031
30. Garbowski, T.; Pawlak, T.G.; Szymczak-Graczyk, A. Efficient load-bearing capacity assessment of a degraded concrete manhole using sectional homogenization. Materials 2024, 17, 5883. https://doi.org/10.3390/ma17235883
31. Pawlak, T.; Szymczak-Graczyk, A.; Garbowski, T. Three-layer repair coating system for manholes, pump stations and tanks in aggressive sulfate environment. Civ. Environ. Eng. Rep. 2025, 35, 1–19. https://doi.org/10.59440/ceer/196751
32. Ksit, B.; Szymczak-Graczyk, A.; Pilch, R. Numerical simulation of the impact of water vapour and moisture blockers in energy diagnostics of ventilated partitions. Materials 2022, 15, 8257. https://doi.org/10.3390/ma15228257
33. Zhang, W.; Gu, X.; Tang, L.; Yin, Y.; Liu, D.; Zhang, Y. Application of machine learning, deep learning and optimization algorithms in geoengineering and geoscience. Gondwana Res. 2022, 109, 1–17.

 doi:10.20944/preprints202602.0160.v1

34. Szymczak-Graczyk, A.; Korentz, J.; Garbowski, T. Digital twin model for predicting hygrothermal performance of building materials from moisture permeability tests. Materials 2025, 18, 4360. https://doi.org/10.3390/ma18184360
35. Cornaggia, A.; Garbowski, T.; Cocchetti, G.; Ferrari, R.; Rizzi, E. Optimised structural modelling for inverse analysis parameter identification relying on dynamic measurements. Eccomass Proceedia 2023, 4234–4248. https://doi.org/10.7712/120123.10715.20669
36. Garbowski, T.; Cocchetti, G.; Cornaggia, A.; Ferrari, R.; Rizzi, E. Inverse analysis investigation by Gaussian processes optimisation of a historical concrete bridge relying on dynamic modal measurements. Eccomass Proceedia 2023, 4249–4264. https://doi.org/10.7712/120123.10716.21212
37. Cornaggia, A.; Ferrari, R.; Zola, M.; Gentile, C. Signal processing methodology of response data from a historical arch bridge toward reliable modal identification. Infrastructures 2022, 7, 74. https://doi.org/10.3390/infrastructures7050074
38. Ferrari, R.; Zola, M.; Cornaggia, A.; Rizzi, E. Advanced signal processing methodology of vibration response data toward structural health monitoring purposes. J. Phys. Conf. Ser. 2024, 2647, 182040. https://doi.org/10.1088/1742-6596/2647/18/182040
39. Thanaraj, D.P.; Arulraj, P.; Al-Jabri, K. Investigation on structural and thermal performance of reinforced concrete beams exposed to standard fire. J. Build. Eng. 2020, 32, 101764. https://doi.org/10.1016/j.jobe.2020.101764
40. Fletcher, I.; Welch, S.; Torero, J.; Carvel, R.; Usmani, A. Behaviour of concrete structures in fire. Therm. Sci. 2007, 11, 37–52. https://doi.org/10.2298/TSCI0702037F
41. Li, Z.; Zhou, X.; Shen, B. Fiber-cement extrudates with perlite subjected to high temperatures. J. Mater. Civ. Eng. 2004, 16, 221–229. https://doi.org/10.1061/(ASCE)0899-1561(2004)16:3(221)
42. Szymczak-Graczyk, A. Rectangular plates of a trapezoidal cross-section subjected to thermal load. IOP Conf. Ser. Mater. Sci. Eng. 2019, 603, 032095. https://doi.org/10.1088/1757-899X/603/3/032095
43. Sayadi, A.; Neitzert, T.R.; Clifton, G.C. Influence of poly-lactic acid on the properties of perlite concrete. Constr. Build. Mater. 2018, 189. https://doi.org/10.1016/j.conbuildmat.2018.09.029
44. Al-Jadiri, R.S.F.; Al-Wahab Ali, M.A.; Frayyeh, Q.J. Study of mechanical and thermal properties of reinforced perlite concrete. Key Eng. Mater. 2022, 924, 233–242.
45. Cornaggia, A.; Boschetti, F.; Mazzotta, C.; Pandolfi, A. Numerical modeling of thermally induced microcracking in porous ceramics using cohesive elements. J. Eur. Ceram. Soc. 2018, 38, 4099–4108. https://doi.org/10.1016/j.jeurceramsoc.2018.04.041
46. Garbowski, T.; Cornaggia, A.; Gajewski, T.; Grabski, J.K.; Mrówczyński, D. Inverse-based multi-step numerical homogenization for mechanical characterization of converted corrugated board. Compos. Struct. 2025, 371, 119701. https://doi.org/10.1016/j.compstruct.2025.119701
47. Babu, K.P.; Mohite, P.M.; Upadhyay, C.S. Development of an RVE and stiffness predictions based on mathematical homogenization theory. Int. J. Solids Struct. 2018, 130–131. https://doi.org/10.1016/j.ijsolstr.2017.10.011
48. Gitman, I.M.; Askes, H.; Sluys, L.J. Representative volume: Existence and size determination. Eng. Fract. Mech. 2007, 74. https://doi.org/10.1016/j.engfracmech.2006.12.021
49. Anoukou, K.; Brenner, R.; Hong, F.; Pellerin, M.; Danas, K. Random distribution of polydisperse ellipsoidal inclusions and homogenization estimates for porous elastic materials. Comput. Struct. 2018, 210. https://doi.org/10.1016/j.compstruc.2018.08.006
50. Dzięcioł, J.; Sas, W. Perspective on application of machine learning algorithms for flow parameter estimation in recycled concrete aggregate. Materials 2023, 16, 1500.
51. Szymczak-Graczyk, A.; Gajewska, G.; Laks, I.; Kostrzewski, W. Influence of variable moisture conditions on thermal conductivity of insulation materials used in passive buildings. Energies 2022, 15, 2626. https://doi.org/10.3390/en15072626
52. Isaksson, P.; Krusper, A.; Gradin, P.A. Shear correction factors for corrugated core structures. Compos. Struct. 2007, 80, 123–130.
53. Hadavinia, H.; Gordnian, K.; Karwatzki, J.; Aboutorabi, A. Deriving shear correction factor for thick laminated plates using the energy equivalence method. Struct. Integr. Durab. 2006, 2, 197–206.

54. Cornaggia, A.; Cocchetti, G.; Buljak, V.; Maier, G. Parameter identification in elastoplastic material models by small punch tests and inverse analysis with model reduction. Meccanica 2018, 53, 3815–3829. https://doi.org/10.1007/s11012-018-0916-9
55. Orbulov, I.N.; Szlancsik, A.; Kemény, A.; Kincses, D. Low-cost lightweight composite metal foams for transportation applications. J. Mater. Eng. Perform. 2022, 31, 6954–6961. https://doi.org/10.1007/s11665-022-06644-4
56. Celik, S.; Family, R.; Menguc, M.P. Analysis of perlite- and pumice-based building insulation materials. J. Build. Eng. 2016, 6, 105–111. https://doi.org/10.1016/j.jobe.2016.02.015
57. Villasmil, W.; Fischer, L.J.; Worlitschek, J. Review and evaluation of thermal insulation materials for thermal energy storage systems. Renew. Sustain. Energy Rev. 2019, 103, 71–84.
58. Ayfari, F.; Hesami, S. Development and evaluation of high-temperature-resistant bituminous composites with expanded perlite and PTFE. Case Stud. Constr. Mater. 2024, 21, e03955. https://doi.org/10.1016/j.cscm.2024.e03955
59. Cornaggia, A.; Cocchetti, G.; Maier, G.; Buljak, V. Inverse structural analyses on small punch tests with model reduction and stochastic approach. In Proc. IEEE Int. Conf. Environ. Electr. Eng. & Ind. Commer. Power Syst. Europe (EEEIC/I&CPS Europe); IEEE: 2018; Art. No. 8494215. https://doi.org/10.1109/EEEIC.2018.8494215
60. Staszak, N.; Szymczak-Graczyk, A.; Garbowski, T. Elastic analysis of three-layer concrete slab based on numerical homogenization with analytical shear correction factor. Appl. Sci. 2022, 12, 9918. https://doi.org/10.3390/app12199918
61. Garbowski, T.; Graczyk, J. Shear correction factor in corrugated board layered plates. Polish Paper Rev. 2025, 81, 686–690. doi: 10.15199/54.2025.12.3
62. Graczyk, J.; Gajewski, T.; Garbowski, T. Shear Correction Factor for Porous Eco-Materials: Mechanical Characterization of a Heterogeneous Medium. *Preprints* **2026**, 2026011251. doi: 10.20944/preprints202601.1251.v1
63. Graczyk, J.; Gajewski, T.; Garbowski, T. Numerical Determination of the Shear Correction Factor for Thin-Walled Steel Sections Using Shell-Based Finite Element Modeling. SSRN 2026 doi: 10.2139/ssrn.6144980